Computational Materials Science 98 (2015) 70–75

Contents lists available at ScienceDirect

Computational Materials Science

journal homepage: www.elsevier.com/locate/commatsci

Transition of mechanisms underlying the rate effects and its significance

Pan Xiao [a,*], Jun Wang [a], Rong Yang [a], Fujiu Ke [b], Yilong Bai [a]

[a] LNM, Institute of Mechanics, Chinese Academy of Sciences, Beijing 100190, China
[b] School of Physics and Nuclear Energy Engineering, Beihang University, Beijing 100191, China

ARTICLE INFO

Article history:
Received 18 September 2014
Received in revised form 28 October 2014
Accepted 31 October 2014
Available online 19 November 2014

Keywords:
Strain rate effect
Molecular dynamics
Thermal activation model
Potential landscapes

ABSTRACT

The strain rate dependency of materials' failure has been widely observed in experiments and simulations, yet its microscopic mechanism is still elusive due to the complexity of failure processes. In this work, modified molecular dynamics simulations are carried out to investigate the strain rate effect over a wide strain rate range. The results demonstrate three typical failure modes induced by the competition of two timescales involved. The transition of mechanisms underlying these failure modes is discussed with a simplified model. The corresponding analysis indicates that the thermal activation model offers a good prediction for the variation of failure strain with respect to applied strain rate for failure mode I; the coupled evolution of atomic motions and potential landscapes governs the failure mode II; and the failure mode III is a result of the rapid separation between loading and deformation parts of the sample.

1. Introduction

The strain rate effect of materials, namely increase of yield stress and strength of materials with an increase in the strain rates, is a key feature in impact and shock dynamics as well as a long standing problem in materials science [1]. The effect has been widely observed in experiments of metals and alloys [2–4]. Experimental results were obtained from different technics [4–6], such as conventional compressive/tensile testing, split Hopkinson pressure bar, shock-determined Hugoniot elastic limit stresses and femtosecond laser pulses [6], over a wide strain rate range from 10^{-4} to almost 10^{9} s^{-1}. Several constitutive models had been proposed to describe the strain, stress and strain-rate relations [7–9]. However, a complete description of the dependency for different materials over such a wide strain rate range is an extremely difficult task. Various mechanisms were introduced to explain the relationship at different strain rate range. For example, it is generally known that for many metals, the dependence of flow stress sharply increases when the strain rate of deformation exceeds about 10^{3}–10^{4} s^{-1} which is interpreted as the consequence of the change in mechanism [10]. Mechanisms such as dislocation generation, deformation twinning, and adiabatic shear banding were proposed to explain the dependency [11,12]. All these mechanisms are very important in understanding the phenomena related to the strain rate effect. However, since most of them are phenomenological explanations, a microscopic or molecular understanding of the effect will provide us new information about basic mechanisms and governing factors.

Molecular dynamics (MD), with its ability to trace the dynamic process of each molecule, has become an orthodox method in elucidating microscopic mechanisms for mechanical behaviors of materials. Lots of MD simulations have been carried out to investigate the strain rate effect of nanoscale structures [13–17]. Besides demonstrating results similar to that observed in experiments, these simulations compensated results at ultrahigh strain rates (above 10^{9} s^{-1}) and revealed much more details such as the evolution of structures at nanoscale. However, the simulated strain rates are limited to be very high, usually above 10^{8} s^{-1} [18]. This limitation is attributed to the intrinsic time scale of femtoseconds in MD, so it is hard to conclude that mechanisms proposed from simulation can be simply extended to that obtained from experiments with strain rates far below 10^{8} s^{-1}. Although efforts have been made to construct multi-timescale or accelerated MD methods [19,20], currently they are not mature for mechanism analysis of strain rate effect. On the other hand, due to the massive degree of freedom and complexity of potential functions, it is hard to quantitatively analyze the strain rate dependency of characteristic stress/strain based on simulation results or applying existing theoretical models, e.g. the thermal activation-strain rate analysis, to the simulation results [8]. Moreover, a deeper understanding of the effect at molecular level can also provide us some helpful clues for designing new multi-timescale methods that may compensate the current MD methods.

* Corresponding author. Tel.: +86 10 82543930.
E-mail address: xiaopan@lnm.imech.ac.cn (P. Xiao).

http://dx.doi.org/10.1016/j.commatsci.2014.10.065
0927-0256/

In this work, we focus on MD simulations to simple atomic systems in order to obtain results with strain rate as low as 10^2 s^{-1} which is close to that measured in experiments. Based on the evolution of atomic motion and potential landscapes, microscopic mechanisms that govern the strain rate effect are discussed. Moreover, competition of multiple timescales involved in the rate effect is also presented.

2. Computational framework

MD simulations were performed on 1-dimensional (1D) atomic chains and 2-dimensional (2D) atomic planes, as illustrated in Fig. 1. These configurations were chosen for two reasons. First, since MD simulations at lower strain rates are quite time consuming, simple configurations make it possible to perform simulations under a wider strain rate range. For example, it takes about one month to simulate the tensile process of an atomic chain containing only 28 atoms under a strain rate of 10^2 s^{-1} on a PC with single CPU (Intel® Core™ i7-3820QM). Unfortunately, the time-related simulation cannot be further accelerated by parallel computation, because adjacent MD steps cannot be performed on different CPUs concurrently. Therefore, if 3-dimensional (3D) atomic systems were considered, the strain rate has to be beyond 10^8 s^{-1} for a tolerable duration which does not meet the requirements for study over wide strain rate range in our work. Second, since we focus on the mechanism of strain rate effect, a simpler system will be enough to reveal the concise physics.

The atomic chain shown in Fig. 1(a) consists of 28 atoms with 4 fixed at each end. The initial length (l_0) is 7.033 nm with interatomic distance $d = 0.2605$ nm. The 2D atomic configuration in Fig. 1(b) represents a close-packed planar crystal with one of its close-packed directions parallel to the x axis. Size of the plane is 20.64×7.74 nm along the x and y directions with the lattice constant $c = 0.258$ nm. As illustrated, the origin of coordinate system for both 1D and 2D configurations is located at the geometric center.

The interatomic interaction is modeled using the Lennard–Jones (L–J) potential

$$\phi = 4e_0\left[\left(\frac{r_0}{r}\right)^{12} - \left(\frac{r_0}{r}\right)^{6}\right], \quad (1)$$

with $e_0 = 0.4912$ eV and $r_0 = 0.23276$ nm [21]. The cutoff radius r_{cut} is set to be 0.7 nm. To reduce the influence of fixed atoms, the length of fixed ends for both atomic chain and plane is chosen to be greater than r_{cut}. Since the L–J potential parameters are fitted for copper, the atomic mass m is set to be 63.546 g/mol in simulations. Actually, embedded-atom method (EAM) potentials are commonly used to model metals and alloys, because they usually predict better results than simple pair wise potentials. In this work, the L–J potential is used for two considerations. First, L–J potentials can also properly model metallic systems even with some defects, such as dislocations, surfaces and interfaces [22]. On the other hand, the failure of atomic systems is an energy competition process (kinetic energy and barriers between different states) which can be investigated using either L–J or EAM potentials. Second, the simple form of L–J potential is suitable for theoretical analysis which will help us extract meaningful physical parameters governing the strain rate effect.

The 1D and 2D systems were firstly equilibrated at a specific initial temperature (T_0) to a stress-free state. Then velocity-controlled loadings were applied. Specifically, a tensile loading is implemented by applying a velocity distribution $v_b x_b/l_0$ to the boundary atoms (where x_b denotes the position of boundary atoms), so the nominal tensile strain rate ($\dot{\varepsilon}$) is v_b/l_0. During simulations, boundary atoms move with the given velocity and the other atoms follow MD steps without any velocity rescaling. Physical quantities (for example, the total energy, temperature and so on) in simulations are extracted by means of time-average statistics. For example, the total resultant force on atoms of the left-side boundary F_L is averaged to characterize the tensile response of the system. Since the yield criterion for most metals is based on the maximum shear stress [23], shearing simulations of the 2D system with a periodic boundary condition imposed along the x-axis under different strain rates are also considered. For shearing simulations, the velocity distribution is applied on boundary atoms along the y-axis.

3. Results

Tensile simulations of the atomic chain were performed under strain rates ranging from 4.28×10^2 to 1.0×10^{12} s^{-1}. Boundary force F_L versus tensile strain ε_t with typical stain rates is plotted in Fig. 2 and three failure modes can be identified.

(I) Smooth elastic stage followed by a catastrophic fracture, e.g. tensile curves for strain rate of 1.13×10^4 and 1.62×10^7 s^{-1}, respectively. In the former case, the atomic chain breaks at 5.46%, which is hereafter denoted by the failure strain ε_f. With the strain rate increasing to 1.62×10^7 s^{-1}, ε_f is enhanced to 6.53%. Observations on fractured atomic configurations show that most of the samples break at regions far away from fixed ends. This failure mode is detected as strain rates are below 10^9 s^{-1}.

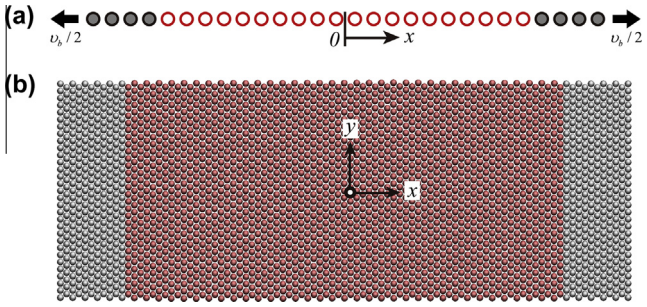

Fig. 1. Configuration for an atomic chain (a) under tensile loading and an atomic plane and (b) used for 2D tensile and shearing simulations. Red atoms are free to move, while boundary atoms (in gray) are manipulated by external velocities. (For interpretation of the references to color in this figure legend, the reader is referred to the web version of this article.)

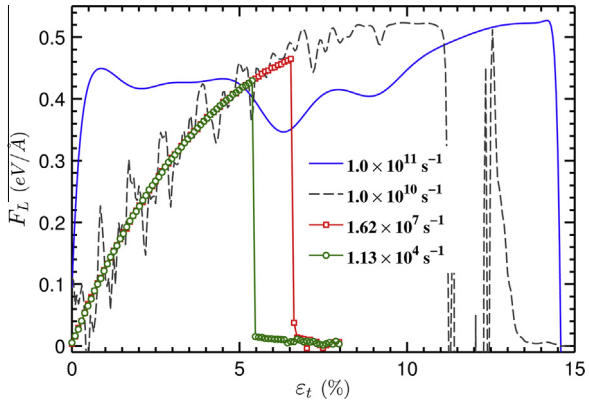

Fig. 2. Variation of boundary forces with tensile strain for atomic chains under various strain rates.

(II) Serrated elastic stage followed by a flow-style failure, e.g. tensile behavior for strain rate of $1.0 \times 10^{10}\ s^{-1}$ in Fig. 2. Although the curve is quite different, the serrated segment at elastic stage is still around that of mode I. Such a failure is seen as strain rates are above $10^9\ s^{-1}$ and below $10^{11}\ s^{-1}$.

(III) Smooth elastic stage followed by a flow-style failure, like the tensile curve for strain rate of $1.0 \times 10^{11}\ s^{-1}$ in Fig. 2. The initial slope of the curve is much higher than that of mode I and ε_f is much larger (13.25%). Atomic chains under strain rates above $10^{11}\ s^{-1}$ undergo such failure mode and always break at the joint of active and fixed atoms.

ε_f for all atomic chains simulated with initial temperature of 50 K are plotted against tensile strain rate in Fig. 3. The results show that ε_f is significantly "strengthened" by strain rate. However, the variation trend of ε_f under strain rates below and above $10^9\ s^{-1}$ is quite different. As the strain rate increases from 10^9 to $10^{11}\ s^{-1}$, ε_f increases 85.33% (from 7.5% to 13.9%). However, it is only enlarged by 38.88% when the strain rate grows from 10^3 to $10^9\ s^{-1}$. This sharp increase of ε_f after a specific strain rate observed in simulations is very similar to that in experiments [10]. Since no additional velocity rescaling is imposed on the atomic system, the statistic temperature varies during loadings. For example, as the atomic chain is stretched under the strain rate of $1.62 \times 10^7\ s^{-1}$, its temperature decreases from the initial 50 K to 21 K when the failure occurs. Further investigation indicates that the reduced kinetic energy and external work done by boundary velocities are used to compensate for the increase of atomic system's potential energy.

Strain rate dependence of ε_f for atomic chains at different temperatures is also investigated. Results plotted in Fig. 4 show that ε_f is strengthened by strain rates with various T_0. Due to the high computational consumption for simulations under low strain rate, only strain rates above $10^4\ s^{-1}$ were considered at temperatures other than 50 K. Both the variation trend of ε_f and its value under the same strain rate are affected by temperature. Specifically, ε_f under a strain rate of $10^4\ s^{-1}$ decreases from 10.85% to 4.35% as T_0 increases from 0 to 100 K. As the strain rate increases from 10^4 to $10^9\ s^{-1}$, ε_f at 1 K changes 8.77% which is much smaller than that of 49.36% at 100 K. It is worth noting that at 0 K ε_f remains 10.85% when strain rates are lower than $10^8\ s^{-1}$. Another interesting result shown in Fig. 4 is that ε_f at 100 K is beyond that at 50 K as ε_t exceeds $10^{10}\ s^{-1}$. Such a phenomenon was reported as the anomalous thermal hardening by Kanel [24] based on their experiments.

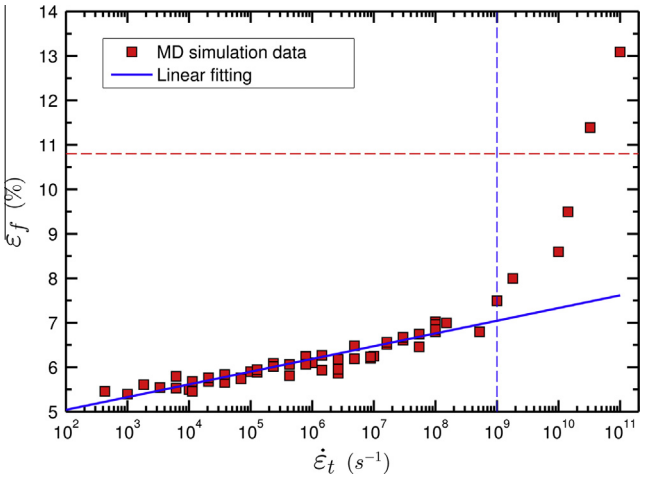

Fig. 3. Tensile failure strain versus strain rate for atomic chains. The blue solid line is obtained by linear fitting to the data below strain rate of $10^9\ s^{-1}$. (For interpretation of the references to colour in this figure legend, the reader is referred to the web version of this article.)

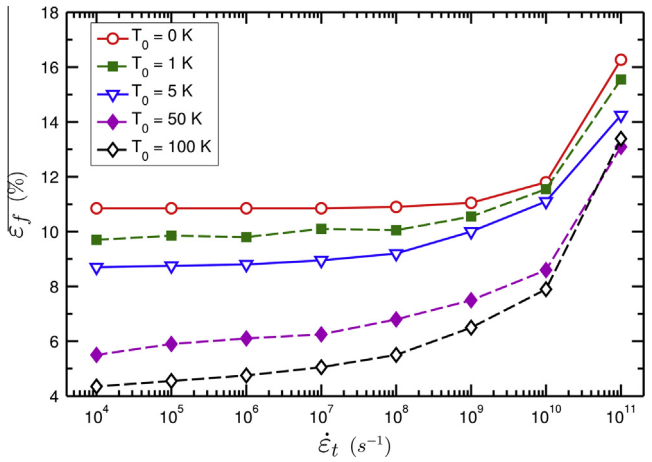

Fig. 4. Tensile failure strain versus strain rate for atomic chains at various temperatures.

Failure behavior of most defect-free crystals (particularly ductile materials) under mechanical loadings is always controlled by nucleation and propagation of dislocations. The dislocation caused failure is, therefore, more sophisticated than the breaking of an atomic chain. So strain rate effect on 2D atomic systems under tension and shearing were also considered to confirm the variation trends obtained from 1D systems. Mechanical responses of atomic planes under various tensile strain rates are quite similar to that of atomic chains, as shown in Fig. 5. The force-strain curves of atomic planes indicate that ε_f is strengthened by strain rates and similar three typical failure modes are also seen. Snapshots in Fig. 6 show the fracture configurations of atomic planes under tensile strain rate of $1.0 \times 10^5\ s^{-1}$, $1.0 \times 10^{10}\ s^{-1}$, $5.0 \times 10^{10}\ s^{-1}$, separately. Configuration observation indicates that the atomic plane failure in Fig. 6(a) (mode I) is caused by sliding along specific directions. With the strain rate increasing, atomic planes undergo a brittle fracture as shown in Fig. 6(b) where the atomic plane breaks into two parts; this is corresponding to failure mode II. Fig. 6(c) sketches mode III in which active atoms separate from fixed boundaries as the atomic plane is stretched with a strain rate higher than $5.0 \times 10^{10}\ s^{-1}$. The failure behavior of mode III is very similar to the breaking of atomic chains.

Variation of ε_f for atomic planes under different tensile and shearing strain rates is also plotted in Fig. 6. Again, the variation trend of atomic planes is similar to that of atomic chains. However the loading strain rates of 2D systems are limited to above

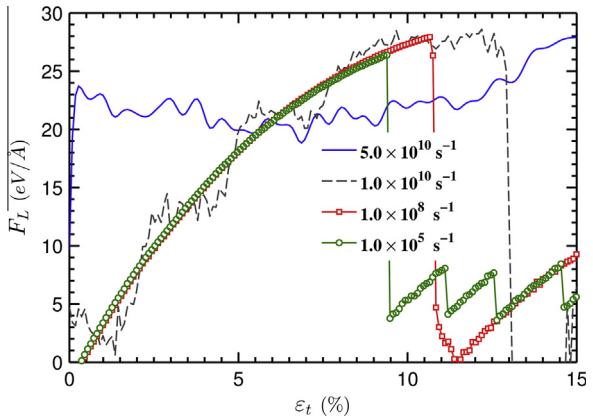

Fig. 5. Boundary forces vary with tensile strain for atomic planes under various strain rates.

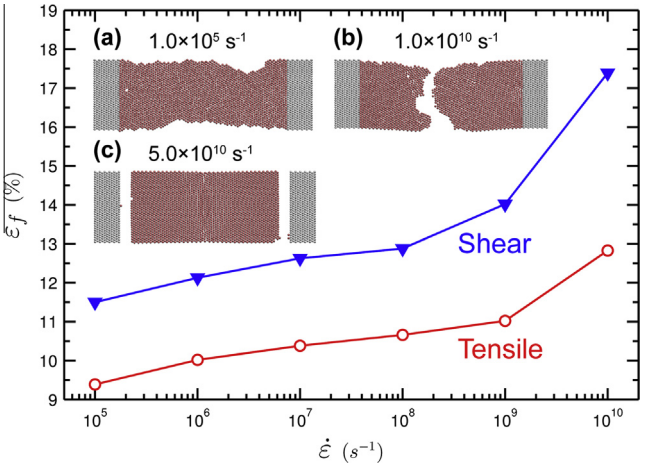

Fig. 6. Failure strain versus strain rate for atomic planes under shear and tensile loadings. Insets are fracture snapshots under various tensile strain rates.

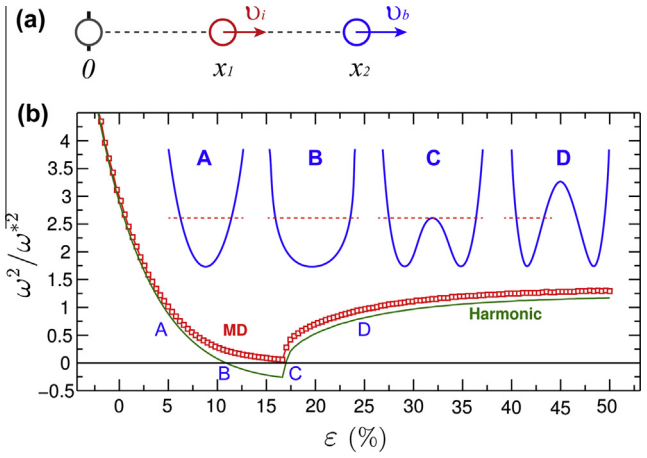

Fig. 7. A 3-atoms model (a) and variation of atomic frequencies (b) with nominal strain obtained from MD simulations and harmonic approximation. Insets show atomic potential landscapes at different strain.

1.0×10^5 s^{-1} due to the increase of atom number. Although strain rates used in 3-D system simulations are always above 1.0×10^8 s^{-1}, similar 3 strain rate regions have been reported previously in MD simulations of 3-D nickel nanowires [15].

4. Discussion

4.1. Timescales involved in the fracture of atomic systems

Both 1D and 2D simulation results show 3 typical failure modes and a distinct transition strain for the dependency of ε_f on strain rate $\dot{\varepsilon}$. To reveal the physics under the phenomenon, we focus on the dependent variables involved in the simulations: timescales. Atomic motion of the simulated systems can be divided into two parts: one is the thermal vibration in potential wells and the other is deformation controlled by external loadings. Generally, characteristic timescales involved in the two parts are quite different and can vary with external conditions. Specifically, the timescale of deformation t_d can be determined by the imposed strain rate, i.e. $1/\dot{\varepsilon}$; while the timescale of thermal vibration is related to the atomic vibration period t_v (the reciprocal of frequency). In this work, the characteristic period t_v^* can be evaluated by the material and potential parameters: $\sqrt{mr_0^2/e_0}$ (about 10^{-13} s). Normally, t_d in experiments is about 1 ms to 1 s which is at least 10 orders of magnitude larger than t_v^*.

While t_d is fixed by a specific strain rate, t_v of an atom can change with strain or the interatomic distance. To make this clear, a simple 3-atoms model is considered, see Fig. 7(a). The 3 atoms are aligned along a straight line with the left one fixed at the origin, the middle one free to move and the right one controlled by external velocity υ_b. Vibration frequency and potential landscape of the free atom are plotted against strain in Fig. 7(b). The atomic frequency at a specific strain marked as MD is calculated from the reciprocal of vibration period which is twice the average time for the free atom moving from the leftmost to rightmost point in MD simulation; while the harmonic approximated frequency is calculated from the second derivative of the potential well at its minimum [25]. The potential landscape at a specific strain is obtained by evaluating potential energies of the free atom at different coordinates around its average position. At point A in Fig. 7(b), the free atom vibrates with a high frequency (or a short period) in its potential well which has only one minimum. As the interatomic distance increases, the potential well becomes wider and atomic frequency decreases. At point B, the second derivative of the potential well at the minimum becomes zero which is indicated by the harmonic approximated frequency. After point B, the potential landscape splits into two minimums at the middle point, yet the free atom have enough kinetic energy to climb over the potential barrier. At point C, atomic kinetic energy almost equal to that of the potential barrier and its frequency is close to zero. It means that the free atom move very slowly with a very long period. After point C, the free atom just vibrates around one of the potential minimums and its frequency increases. Therefore, during the tensile process, t_d remains the same while t_v changes dramatically due to the evolution of atomic potential landscape.

Point C in Fig. 7(b) is a singularity for the 3-atoms model and can be analogous to the failure strain of atomic chains. Evolution of atomic potential landscape in strain region near point C is quite critical for the failure of atomic system. Let us take a small strain region $\Delta\varepsilon_C = 1\%$ before point C for consideration. Frequency of the middle atom at $\varepsilon_C - \Delta\varepsilon_C$ decreases to less than 0.1 of the characteristic frequency, or t_v is about 10^{-12} s. On the other hand, t_d over the region will be $\Delta\varepsilon_C/\dot{\varepsilon}$. When the loading strain rate is rather slow, e.g. $\dot{\varepsilon}$ in failure mode I, t_d (>10^{-10} s) is much longer than t_v. Therefore the middle atom has enough time to adjust its thermal vibration in order to adapt the change of potential landscapes. Then the failure of atomic system will be controlled by kinetic energy of the middle atom and the height of potential barrier. For the other extreme, e.g. $\dot{\varepsilon}$ in mode III with strain rate faster than 10^{11} s^{-1}, t_d (<10^{-13} s) is shorter than t_v. For this case, there is no sufficient time for the middle atom to finish a complete thermal vibration within the time of t_d. That is, the middle atom will fail to "feel" the rapid movements of the right atom after the interatomic distance exceeds r_{cut}. So failure is dominated by the external velocity which determines the time when the interatomic distance between the middle and right atoms reach to r_{cut}. That is why mode I failure of 2D atomic systems shows atomic sliding in the free region while mode III shows brittle fracture at the interface between active and fixed atoms, see Fig. 6(a) and (c). Finally for mode II with strain rates between that of mode I and III, t_d is comparable to t_v over region $\Delta\varepsilon_C$, then coupling of the atomic thermal vibration and evolution of potential landscape plays an important role. Consequently, failure mode II in Fig. 6(b) demonstrates a more complicated fracture character mixed with that of both modes I and III. It is the competition between t_d and t_v that lead to the transition of failure modes and mechanisms. Specifically, mechanisms underlying the rate effect with failure modes I and II are discussed in details.

4.2. Thermal activation explanation to failure mode I

Since t_d is much longer than t_v for mode I, fracture of atomic chains can be determined by the current kinetic energy and potential barrier. In other words, an atomic chain will break if it has enough kinetic energy to climb over the potential barrier. It is a typical thermal activation process and a dependence of ε_f on $\dot{\varepsilon}$ can be established using the Arrhenius-type equation [26]

$$\dot{\varepsilon}_f = \dot{\varepsilon}_0 e^{-\frac{\Delta U(\varepsilon)}{kT}}, \tag{2}$$

where $\dot{\varepsilon}_f$ is the failure strain rate [16,26,27]; $\dot{\varepsilon}_0$ is a pre-exponential constant or a characteristic strain rate; ΔU is the activation energy for failure which is a function of the current strain ε; k is the Boltzman constant and T is the absolute temperature. A similar postulation used in [16] is introduced: when $\dot{\varepsilon}_f$ equals the imposed strain rate $\dot{\varepsilon}$, the atomic system will failure and can no longer support loads, i.e.,

$$\dot{\varepsilon}_f \approx \dot{\varepsilon}. \tag{3}$$

Then Eq. (2) can be rewritten and $\dot{\varepsilon}$ can be connected with the failure strain ε_f as

$$\dot{\varepsilon} = \dot{\varepsilon}_0 e^{-\frac{\Delta U(\varepsilon_f)}{kT}}, \tag{4}$$

where $\Delta U(\varepsilon_f)$ is the activation energy at ε_f. In order to evaluate $\Delta U(\varepsilon_f)$, an atomic chain with periodic boundary condition and described with the L–J potential of Eq. (1) is considered. If the interatomic distance is a_0 when the atomic chain is at stress-free state, then the per-atom potential energy (summation of L–J potentials over all neighbors of an atom) at strain ε is

$$\phi(\varepsilon) = C_{12}(1+\varepsilon)^{-12} - C_6(1+\varepsilon)^{-6}, \tag{5}$$

where $C_{12} = 4e_0\left(\frac{r_0}{a_0}\right)^{12}\sum_{n=1}^{\infty}\frac{1}{n^{12}}$ and $C_6 = 4e_0\left(\frac{r_0}{a_0}\right)^{6}\sum_{n=1}^{\infty}\frac{1}{n^{6}}$ are summation constants. The stress-free interatomic distance a_0 can be determined by condition

$$\phi'(0) = -12C_{12} + 6C_6 = 0 \tag{6}$$

which can be numerically evaluated as $a_0 = 1.1193r_0$. Therefore, $\Delta U(\varepsilon_f)$ can be calculated as the difference between per-atom potential energy at ε_f and the unstable strain ε_m for the atomic chain:

$$\Delta U(\varepsilon_f) = \phi(\varepsilon_m) - \phi(\varepsilon_f). \tag{7}$$

where ε_m can be determined by the unstable condition

$$\phi''(\varepsilon_m) = 0. \tag{8}$$

Combining the second derivative of Eqs. (5) and (8), we can get $\varepsilon_m = 10.87\%$. This value agrees well with the simulation results of ε_f for atomic chain at 0 K which remains about 10.85% when strain rates are slower than 10^8 s^{-1}. ε_m can also be understood as the theoretic failure strain or the ceiling of ε_f for atomic chains with failure mode I. Since ε_f of mode I in Fig. 3 is approaching to ε_m, Eq. (5) can be Taylor expanded near ε_m:

$$\phi(\varepsilon) = \phi(\varepsilon_m) + \phi'(\varepsilon_m)(\varepsilon-\varepsilon_m) + \frac{1}{2}\phi''(\varepsilon_m)(\varepsilon-\varepsilon_m)^2 + o((\varepsilon-\varepsilon_m)^2). \tag{9}$$

Recalling Eq. (8), we can get the second-order approximation of $\phi(\varepsilon)$ around ε_m as

$$\phi(\varepsilon) \approx \phi(\varepsilon_m) + \phi'(\varepsilon_m)(\varepsilon-\varepsilon_m). \tag{10}$$

So the activation energy in Eq. (7) can be approximated as

$$\Delta U(\varepsilon_f) \approx \phi'(\varepsilon_m)(\varepsilon_m - \varepsilon_f). \tag{11}$$

By substituting Eq. (11) into Eq. (4), finally we get an approximated relationship between ε_f and $\dot{\varepsilon}$:

$$\varepsilon_f = \frac{kT}{\phi'(\varepsilon_m)}(\ln\dot{\varepsilon} - \ln\dot{\varepsilon}_0) + \varepsilon_m \tag{12}$$

Eq. (12) indicates that ε_f is proportional to temperature T which is consistent with the MD results obtained above. Moreover, Eq. (12) also shows that ε_f is linear proportional to $\ln\dot{\varepsilon}$ with a slope of $kT/\phi'(\varepsilon_m)$. Specifically, for the atomic chains with initial temperature of 50 K, the slope is evaluated to be 1.324×10^{-3} which is well consistent with that, 1.243×10^{-3}, fitted with the simulation data in Fig. 3, with a minor error less than 6%. It should be mentioned that since temperature of the system decreases from 50 to 21 K during tension, the theoretical slope is calculated using the temperature of 21 K which reflects the amount of kinetic energy to overcome the potential barrier at ε_f. According to Eq. (12), the slope goes to zero and ε_f remains ε_m at 0 K which is consistent with the simulation result in Fig. 4. These results indicate that the thermal activation model shows a good competence for the explanation of strain rate effect with failure mode I observed in MD simulations.

4.3. Coupled evolution of atomic motions and potential landscapes

As mentioned above, failure mode II of atomic systems is controlled by the coupling of two timescales; and it is hard to be theoretically analyzed. In order to clarify the mechanism involved, the 3-atoms model is employed again to extract a phenomenological explanation. Fig. 8 shows trajectories of the middle atom in potential landscapes under various boundary velocities v_b.

The 3D landscape in Fig. 8 is generated by calculating the potential energies of the free atom at different positions (x coordinates) and strains (ε). It can be seen that the atomic potential landscape splits at a critical strain ε_{cr} (similar to ε_m of an atomic chain). After ε_{cr}, the atom slips into one of the two minimums and vibrates in a new potential well. For failure mode II, the force-drop strain ε_{drop} (equivalent to ε_f of an atomic chain) observed in the strain-force curve of 3-atoms model is corresponding to the strain at which the atom locates at the new local minimum of potential landscape (see insets in Fig. 9). Since the atomic frequency near ε_{cr} approaches to zero (point C in Fig. 7), the middle atom can move with a very slow velocity which is comparable to the external velocity v_b. As a result, a "dragging effect" by v_b is acted on the movement of the middle atom. At the moment, the coupled evolu-

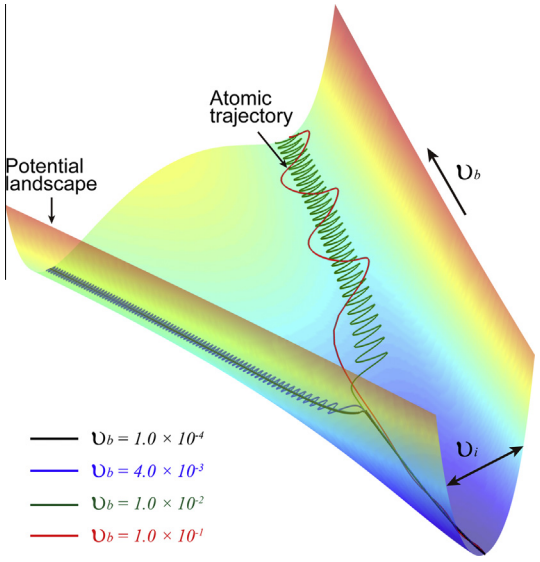

Fig. 8. Atomic trajectories in potential landscape under various boundary velocities (v_b) for a 3-atoms model.

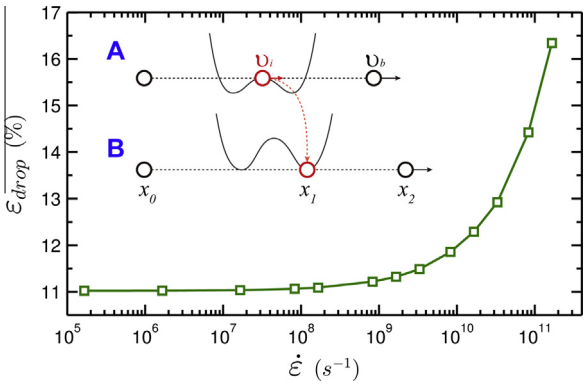

Fig. 9. Force-drop strain as a function of strain rate for a 3-atoms model. Insets illustrate an atom moves from the "hilltop" to the "valley bottom" of a potential landscape during tensile process.

tion of atomic motions and potential landscapes becomes a dominant and a faster υ_b leads to a greater ε_{drop}, see Fig. 8. In other words, for mode II, the faster $\dot{\varepsilon}$ is applied, the greater ε_f will be obtained from the strain-force curve. Due to different mechanisms, the incensement of ε_f with $\dot{\varepsilon}$ for mode II can be faster than that of mode I. ε_{drop} of the 3-atoms model is plotted against $\dot{\varepsilon}$ in Fig. 9. The $\dot{\varepsilon}$ dependency of ε_{drop} is quite similar to that of atomic chain simulations with failure mode II in Figs. 3 and 4. It is worth noting that ε_{drop} is greater than $\varepsilon_{cr} = 10.87\%$. Similarly in the simulation of atomic chains, we can get ε_f greater than ε_m (see Fig. 2) and it is also a result of the coupling effect. Moreover, we can predict that a fast υ_i in Fig. 9 at a high temperature will lead to a large ε_{drop}. Thus the anomalous thermal hardening phenomenon mentioned in Section 3 can be observed.

5. Conclusions

The strain rate effect commonly observed in experiments is analyzed using MD simulations. Models including a 1D atomic chain, a 2D atomic plane and a 3-atoms system are examined to clarify fundamental mechanisms underlying the strain rate effect. Tensile deformation of the 1D atomic chain certifies the strain rates ($\dot{\varepsilon}$) dependency of failure strain (ε_f), with $\dot{\varepsilon}$ ranging from 4.28×10^2 to $1.0 \times 10^{12}\,s^{-1}$. Three typical failure modes with different mechanical responses are detected. The strain rate dependency is also confirmed in the tensile and shear simulations of 2D atomic planes. Analysis combining simulation results and a 3-atoms model manifests that two characteristic timescales, the timescale of atomic thermal vibration (t_v) and external deformation (t_d), are involved in the strain rate effect. It is found that although t_d may remain unchanged during a loading process, t_v can dramatically change with the evolution of potential landscapes. It is the competition of the two timescales that lead to the three failure modes and transition of mechanisms. Specifically, for failure mode I with t_d much longer than t_v, the thermal activation theory shows a good competence for explaining the strain rate dependency. The theory indicates that ε_f of atomic chains shows a linear dependency on $\ln\dot{\varepsilon}$ with a slop of $kT/\phi'(\varepsilon_m)$. The evaluated theoretical slop shows well consistent with simulated data. For failure mode II with t_d comparable to t_v, the coupled evolution of atomic motions and potential landscapes becomes a dominant for the dependency of ε_f on $\dot{\varepsilon}$. Finally for the failure mode III with t_d shorter than t_v, the failure is a result of the rapid separation between loading and deformation parts of the atomic system.

Acknowledgements

Support from the National Basic Research Program of China (Grant No. 2012CB937500), the National Natural Science Foundation of China (Grant Nos. 11202212, 11172305, 11172024, 11232013 and 11372022), is gratefully acknowledged. Computations were performed on the ScGrid of Supercomputing Center, Computer Network Information Center of Chinese Academy of Sciences and LNMGrid of the State Key Laboratory of Nonlinear Mechanics.

References

[1] R.W. Armstrong, S.M. Walley, Int. Mater. Rev. 53 (2008) 105.
[2] S.C. Chou, K.D. Robertson, J.H. Rainey, Exp. Mech. 13 (1973) 422.
[3] J.W. Swegle, D.E. Grady, J. Appl. Phys. 58 (1985) 692.
[4] R.W. Armstrong, W. Arnold, F.J. Zerilli, Metall. Mater. Trans. A 38 (2007) 2605.
[5] R. Liang, A.S. Khan, Int. J. Plast 15 (1999) 963.
[6] S.I. Ashitkov, M.B. Agranat, G.I. Kanel, P.S. Komarov, V.E. Fortov, JETP Lett. 92 (2010) 516.
[7] A.S. Khan, S. Huang, Int. J. Plast 8 (1992) 397.
[8] F.J. Zerilli, R.W. Armstrong, J. Appl. Phys. 61 (1987) 1816.
[9] G.R. Johnson, W.H. Cook, Proc. 7th Int. Symp. Ballist., vol. 547, 1983, pp. 541.
[10] S.V. Razorenov, G.I. Kanel, G.V. Garkushin, O.N. Ignatova, Phys. Solid State 54 (2012) 790.
[11] L.E. Murr, E.V. Esquivel, J. Mater. Sci. 39 (2004) 1153.
[12] L.E. Murr, M.A. Meyers, C.S. Niou, Y.J. Chen, S. Pappu, C. Kennedy, Acta Mater. 45 (1997) 157.
[13] H.A. Wu, Comput. Mater. Sci. 31 (2004) 287.
[14] S.J.A. Koh, H.P. Lee, C. Lu, Q.H. Cheng, Phys. Rev. B 72 (2005) 85414.
[15] Y.H. Wen, Z.Z. Zhu, R.Z. Zhu, Comput. Mater. Sci. 41 (2008) 553.
[16] N. Wagner, B. Holian, A. Voter, Phys. Rev. A 45 (1992) 8457.
[17] Y.M. Wang, E. Ma, Appl. Phys. Lett. 83 (2003) 3165.
[18] K. Kadau, P.S. Lomdahl, B.L. Holian, T.C. Germann, D. Kadau, P. Entel, D.E. Wolf, M. Kreth, F. Westerhoff, Metall. Mater. Trans. A 35 (2004) 2719.
[19] P. Xiao, J. Wang, R. Yang, F.J. Ke, M.F. Xia, Y.L. Bai, Acta. Mech. Sin. 29 (2013) 676.
[20] A.F. Voter, F. Montalenti, T.C. Germann, Annu. Rev. Mater. Res. 32 (2002) 321.
[21] R. Najafabadi, D.J. Srolovitz, Phys. Rev. B 52 (1995) 9229.
[22] H. Heinz, R.A. Vaia, B.L. Farmer, R.R. Naik, J. Phys. Chem. C 112 (2008) 17281.
[23] C.A. Schuh, A.C. Lund, Nat. Mater. 2 (2003) 449.
[24] G.I. Kanel, AIP Conf. Proc. 1426 (2012) 939.
[25] R. LeSar, R. Najafabadi, D.J. Srolovitz, Phys. Rev. Lett. 63 (1989) 624.
[26] Q. Wei, J. Mater. Sci. 42 (2007) 1709.
[27] Y.M. Wang, A.V. Hamza, E. Ma, Acta Mater. 54 (2006) 2715.